

Effect of doping on electronic structure and photocatalytic behavior of amorphous TiO₂

This content has been downloaded from IOPscience. Please scroll down to see the full text.

2013 J. Phys.: Condens. Matter 25 475501

(<http://iopscience.iop.org/0953-8984/25/47/475501>)

View [the table of contents for this issue](#), or go to the [journal homepage](#) for more

Download details:

IP Address: 128.100.25.116

This content was downloaded on 10/11/2014 at 15:04

Please note that [terms and conditions apply](#).

Effect of doping on electronic structure and photocatalytic behavior of amorphous TiO₂

Kulbir Kaur Ghuman and Chandra Veer Singh

Department of Materials Science and Engineering, University of Toronto, 184 College Street, Suite 140, Toronto, ON M5S 3E4, Canada

E-mail: chandraveer.singh@utoronto.ca

Received 24 July 2013, in final form 27 September 2013

Published 31 October 2013

Online at stacks.iop.org/JPhysCM/25/475501

Abstract

Visible light photocatalysts based on doped crystalline forms of titanium dioxide (TiO₂) have attracted significant scientific attention in recent decades. Amorphous TiO₂, despite many merits over crystalline phases, has not been studied as thoroughly. In this paper, an in-depth analysis of the electronic properties of doped amorphous TiO₂ is performed using density functional theory with Hubbard's energy correction (DFT + *U*). Monodoping with p-type (N) and n-type (Nb) dopants shows appreciable bandgap reduction, but leads to recombination centers due to the presence of uncompensated charges. To resolve this issue, charge compensation via codoping is attempted. The charge compensated codoping not only reduces the bandgap by 0.4 eV but also eliminates the bandgap states present in monodoped systems responsible for charge carrier recombination. Furthermore, the localized tail states present in the aTiO₂ system are eliminated to a large extent which leads to a decrease in the charge recombination and an increase in the charge migration. Thus, appropriate doping of amorphous TiO₂ may lead to an alternative route for the development of visible light photocatalysts.

(Some figures may appear in colour only in the online journal)

1. Introduction

The exceptional physicochemical properties of crystalline forms of titanium oxide (cTiO₂) such as high thermal and chemical stability, high photocatalytic activity, low-toxicity and relatively low cost have attracted significant attention for photocatalytic research. Amorphous titania (aTiO₂), on the other hand, has been mostly neglected for such applications due to a relatively wide bandgap, large disorder and a high concentration of imperfections. The defects such as impurities, dangling bonds, and microvoids present in aTiO₂ typically leads to unwanted electronic states in the bandgap that result in the reduction of charge migration and a rapid recombination of electron-hole pairs (Rahman *et al* 2011, Ohtani *et al* 1997, Mott and Davis 1979). These disadvantages have overshadowed particularly interesting characteristics of aTiO₂ that may make it more advantageous over crystalline forms in practical applications. For instance, aTiO₂ has a

larger surface area than cTiO₂ which leads to a higher absorptivity. It is also more widely available in nature and can be prepared at room temperature. In addition to this, being isotropic in nature, it has optical properties that are independent of the direction of the incident light (Prasai *et al* 2012). Finally, the amorphous form is more amenable to processing into various forms which allows doping with a wider range of dopants.

Due to the above characteristics, there has been a renewed interest in recent years in developing aTiO₂ as an alternative photocatalyst to cTiO₂ (Prasai *et al* 2012, Zhang and Maggard 2007, Li *et al* 2008, Kanna and Wongnawa 2008, Buddee *et al* 2011, Kaur and Singh 2012). Some studies have already shown aTiO₂ to be better than the crystalline forms for a variety of applications. For example, aTiO₂ dye sensitized solar cell exhibits higher efficiency than a nanocrystalline TiO₂ layer (Han *et al* 2009). Experimental investigation by Buddee *et al* (2011) reported that Fe/Cr

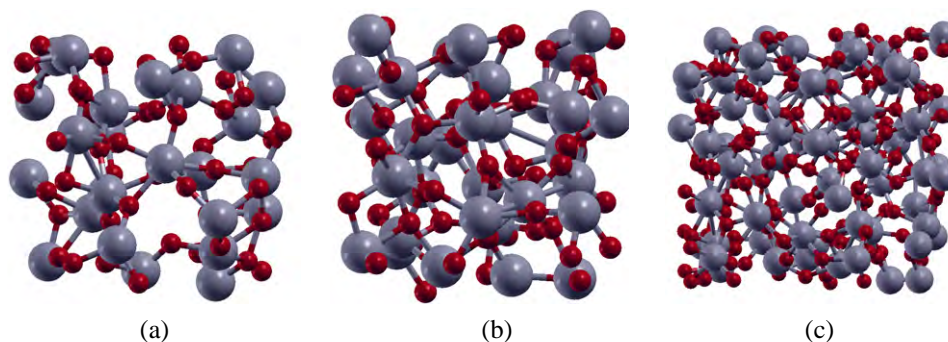


Figure 1. Relaxed structures of (a) 72-atom, (b) 96-atom and (c) 216-atom models of amorphous TiO_2 . The red and gray spheres represent O and Ti atoms, respectively.

doped aTiO_2 shows enhanced photocatalytic activity under both UV and visible light spectra. Their study also found that the aTiO_2 photocatalyst can be used endlessly without any detrimental effect on the photocatalytic efficiency. This long-life photocatalytic performance is a significant advantage of aTiO_2 over cTiO_2 . Hence, structural disorder present in aTiO_2 may not be essentially detrimental for photocatalysis. As exemplified in a remarkable study by Chen *et al* (2011), it is now possible to *defect engineer* TiO_2 nanocrystals to yield controlled mid-gap states arising out of structural disorder that reduce the bandgap and lead to significant improvement in visible light photocatalytic performance. aTiO_2 represents one extreme example of a disordered structure that, if understood and manipulated carefully, can lead to more cost-effective and efficient photocatalysts.

This paper is focused on a theoretical investigation of the effects of n-type, p-type and charge compensated codoping on the electronic properties of aTiO_2 . Amorphous samples were prepared using the melt-and-quench method via classical molecular dynamics (MD) simulations. Multiple sized samples were considered for understanding the supercell size effects. The electronic properties were then computed using the DFT + U methodology for undoped, monodoped, and codoped aTiO_2 systems. The state of disorder for the amorphous phase consisting of localized defect states, and its effect on the resultant electronic structure were understood by analyzing the variation of *inverse participation ratio* (IPR). The electronic band structures of aTiO_2 systems were also compared to the crystalline phases. Since the beneficial aspects of doping cTiO_2 with p-type, n-type and mixed type dopants have already been established (Ma *et al* 2011, Tsetseris 2011, Morgan *et al* 2009), we attempted doping of aTiO_2 in a similar manner. It was found that while monodoping of aTiO_2 with N or Nb decreases the bandgap, it leads to localized defect states in the band structure. These localized defect states may act as sites for the recombination of charge carriers and thus detrimentally affect the photocatalytic efficiency. In order to overcome this challenge, charge compensated codoping was performed. The resultant system showed improved electronic structure as compared to undoped and N/Nb monodoped aTiO_2 for photocatalysis. This is due to a reduction in the localized

and the mid-bandgap states which might be responsible for formation of recombination centers and reduced charge migration.

2. Computational details

In order to prepare and understand the electronic structure and photocatalytic properties of aTiO_2 , a combination of classical MD and DFT was utilized. Amorphous samples were prepared using the melt-and-quench method via MD simulations through DLPOLY (Smith and Todorov 2006) using periodic boundary conditions. Multiple supercell sizes of 72, 96 and 216 atoms (figure 1) were considered to analyze and understand the size effects on the electronic properties of aTiO_2 . The Matsui–Akaogi force field (Matsui and Akaogi 1991) was used for calculating the short range interactions; and the effect of long range Coulomb interactions was taken into account using the *Damped Shifted Force Coulomb Sum* method (Fennell and Gezelter 2006). Initial configurations of the three samples were chosen with a side length obtained by rescaling the crystalline configurations of the rutile phase so as to have the mass density of the resultant systems matching that of aTiO_2 , i.e. 3.8 g cm^{-3} . Each sample was first subjected to a geometric optimization and then heated up to a temperature greater than the melting point of TiO_2 ($T = 2116 \text{ K}$) for eliminating the initial memory of the structure. Thereafter, sequential heating and quenching cycles were performed, each followed by equilibration of the resultant systems for sufficiently long time to ensure that they attain steady state. Finally, the samples were relaxed to 0 K. The samples obtained from MD were further relaxed to achieve their ground state configurations using DFT computations before calculating their structural and electronic properties. Further details of the sample preparation procedure and structural properties of the three aTiO_2 samples have been presented in our earlier report (Kaur and Singh 2012).

The DFT methodology under-predicts the bandgap and delocalization of d and f electrons for semiconductors like TiO_2 . The DFT + U approach, followed here, adds an energy correction term U to the DFT energy and leads to a more accurate bandgap as well as the localization of d and f electrons consistent with physical observations. Since the focus here is on electronic properties, the value of U

parameter was chosen based on the position of the bandgap states of crystalline rutile (Ghuman and Singh 2013). Due to a lack of experimental data for aTiO₂, the same value of U is assumed to hold for aTiO₂. Spectroscopic experiments for bulk reduced rutile TiO₂ crystals have suggested a broad gap state lying about 0.9 eV below the conduction band (CB) edge (Wendt *et al* 2008, Thomas *et al* 2007). Following the approach of Möller *et al* (2010), it was found that $U = 4.2$ eV yields the correct position of bandgap states due to Ti interstitial and O vacancy defects, while opening up the bandgap to 2.2 eV for rutile. This value of U is also consistent with theoretical investigations by Morgan and Watson (2007), who calculated it by fitting the peak positions for surface oxygen vacancies to experimental XPS data.

The Quantum Espresso (Giannozzi *et al* 2009) software package within the plane-wave pseudopotential approach was utilized throughout this study. Interactions between the valence electrons and the ionic core were represented by the Vanderbilt ultra-soft pseudopotential (Vanderbilt 1990) and the electron–electron correlation was approximated by the generalized gradient approximation (GGA) in the Perdew–Burke–Ernzerhof (PBE) formulation (Perdew *et al* 1996). The kinetic energy cutoffs of 540 eV and 5400 eV were used for the wavefunctions and the charge density, respectively. Brillouin zone integrations were performed using a Monkhorst–Pack (Monkhorst and Pack 1976) grid of $4 \times 4 \times 6$, $4 \times 4 \times 6$ and $1 \times 1 \times 2$ k -points for the 72, 96 and 216-atom models, respectively. Due to the large size of the 216-atom model, a coarse k -grid was considered sufficient. A fine k -grid for this sample would incur huge computational cost and is currently beyond the scope of this study. All calculations were spin polarized. The structures were relaxed using a conjugate gradient minimization algorithm until the magnitude of the residual Hellman–Feynman force on each atom was less than 10^{-3} Ryd/bohr. While plotting the total density of states (DOS) and projected density of states (PDOS) (Sanchez-Portal *et al* 1995), a conventional Gaussian smearing of 0.1 eV was utilized.

3. Results and discussion

3.1. Structural and electronic properties of undoped aTiO₂

Electronic structure and, consequently, the photocatalytic properties of amorphous systems are intrinsically dependent on the short range structural disorder, which depends on the specific material type, growth process and previous history. Thus, it is of utmost importance to perform *ab initio* calculations over amorphous structures that correspond well with experimental observations. In order to verify the accuracy of prepared samples, structural properties were investigated and compared to the available experimental data (Petkov *et al* 1998, Manzini *et al* 1995, Rino and Studart 1999). The detailed results are available in our earlier report (Kaur and Singh 2012). To summarize, it was found that the structural properties of aTiO₂ obtained from *ab initio* calculations agree very well with experiments. Most of the Ti and O atoms in amorphous samples tend to remain six-fold

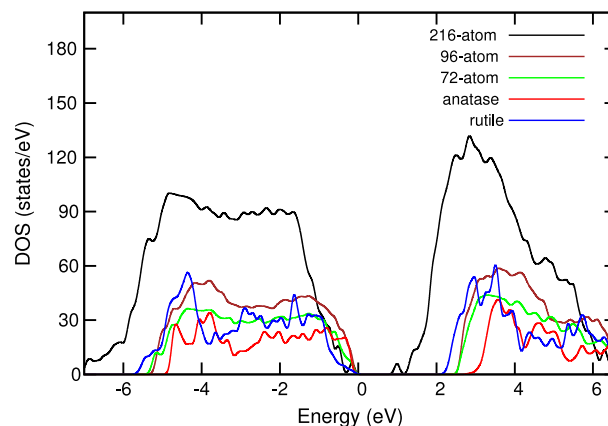


Figure 2. Total density of states for crystalline and amorphous TiO₂ systems obtained by using DFT + U .

and three-fold, respectively, similar to the case of cTiO₂. However, a large number of Ti–O bonds become compressed, whereas a few are stretched in comparison to cTiO₂. The planar orientation, represented by the distribution of dihedral angles, becomes nearly random for amorphous samples, in agreement with other computational studies of aTiO₂ (Kaur *et al* 2011).

Once the aTiO₂ samples were validated for their amorphicity and local structure, the electronic properties were investigated using the DFT + U approach. The DOS for all three models of aTiO₂ along with that of rutile of supercell size $2 \times 2 \times 3$ (72 atoms) and anatase of supercell size $2 \times 2 \times 2$ (48 atoms) are shown in figure 2. On closer examination of the PDOS of these models (figures are not shown for 72 and 96-atom models), some differences were observed in the location and the width of energy states. The CB and VB are dominated by the Ti 3d states and O 2p states, respectively, in all the models. This behavior is similar to both crystalline phases. The PDOS for the 96-atom aTiO₂ model is shown in figure 3(a). The magnitude of the Γ point electronic gap, defined as the difference between the highest occupied molecular orbital (HOMO) and the lowest unoccupied molecular orbital (LUMO), for all models is tabulated in table 1. The corresponding experimental data (Amtout and Leonelli 1995, Tang *et al* 1993, Valencia *et al* 2010) are also shown for comparison. It can be seen that the Γ point electronic bandgap values for 72-atom and 96-atom models are comparable to anatase. This is consistent with the investigation on aTiO₂ by Prasai *et al* (2012). However, the 216-atom model is found to have a very small Γ point bandgap, which is due to the presence of a larger number of tail states in the mobility bandgap as compared to the 72- and 96-atom models. As explained by Fedders *et al* (1998), this could be an artifact due to the presence of dangling bonds, and can be corrected by eliminating atoms associated with the dangling bonds. For the discussion here, the 96-atom model is focused on.

Amorphous material is known to have a low photocatalytic efficiency, mainly due to the localization of the tail states near the bandgap in contrast to the completely delocalized tail states in a crystalline material. This reduces the

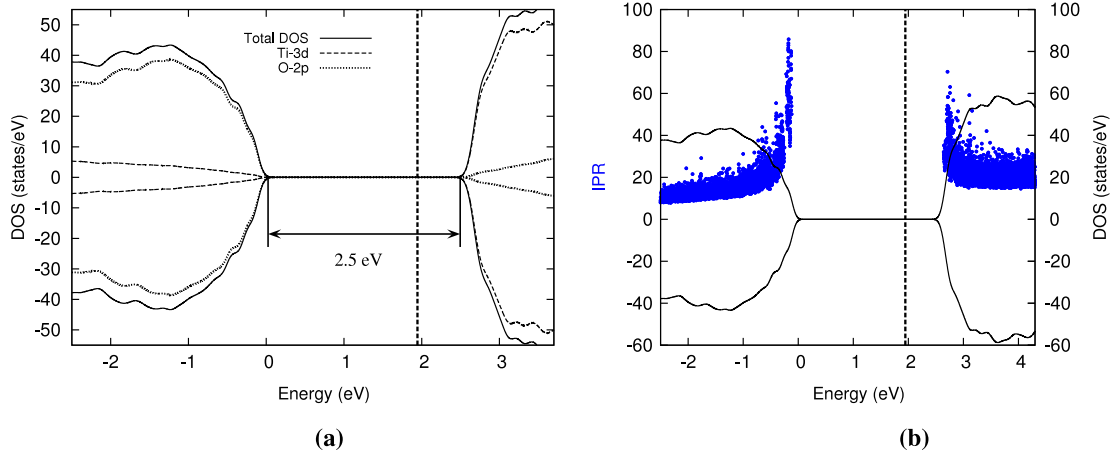


Figure 3. (a) The density of states projected on the p and d orbitals and (b) the total density of states (black line, right scale) and the corresponding values of the inverse participation ratio (IPR) (blue dots, left scale) for undoped 96-atom aTiO₂ model. The zero energy value is set at the top of VB and the Fermi energy is represented by the vertical dashed line.

Table 1. A comparison of calculated and experimental band gaps for crystalline TiO₂ and amorphous TiO₂.

Bandgap (eV)	Crystalline TiO ₂		Amorphous TiO ₂					
	Rutile Γ point	Anatase Γ point	72-atom		96-atom		216-atom	
	Γ point	Γ point	Γ point	IPR	Γ point	IPR	Γ point	IPR
Calc. (DFT)	1.782	2.532	2.1	2.85	2.1	2.8	0.8	2.5
Calc. (DFT + U)	2.20	2.50	2.5	3.2	2.5	3.0	1.0	2.8
Expt.	3.03 (Amtout and Leonelli 1995)		3.20 (Tang <i>et al</i> 1993)		3.4 (Valencia <i>et al</i> 2010)			

charge mobility and increases the number of recombination centers in aTiO₂. To investigate this localization of the tail states and to obtain the mobility bandgap, IPR analysis was performed following the procedure suggested by Justo *et al* (2002). The IPR of an orbital $\psi_n(\vec{r}_i)$, $I(\psi_n)$, is accordingly defined by

$$I(\psi_n) = N \frac{\sum_{i=1}^N |\psi_n(\vec{r}_i)|^4}{[\sum_{i=1}^N |\psi_n(\vec{r}_i)|^2]^2} \quad (1)$$

where N is the number of volume elements in the cell, and i is the index of the volume element. The IPR is large for highly localized states, and small for delocalized states. Ideally, a localized orbital means $I(\psi) = N$, whereas a delocalized orbital means $I(\psi) = 1$. The IPR can identify a level as belonging to the delocalized band, to the partially localized band tail, or to the highly localized bandgap. Thus IPR analysis provides a reasonable method to understand the localization of energy states. The band tail electronic states, shown in figure 3(b), were found to be strongly localized in all three aTiO₂ models, consistent with other disordered systems such as amorphous carbon (Stumm and Drabold 1996). As results are similar for the different aTiO₂ models, only the plots for the 96-atom model are shown in figure 3. From the figure, it is observed that the valence tail states are more localized as compared to the conduction tail states. This is consistent with the observations of Prasai *et al* (2012). The large IPR for the states in the bottom of CB and the top of VB is a result of the localized character of the Ti 3d and O 2p states.

IPR analysis can also be used for bandgap prediction by analyzing the change in degree of localization of electronic states near the VB and CB edges, as provided in table 1. The bottom of the CB and the top of the VB were determined as the energy levels where the IPR becomes larger than the average IPR of levels at few eV above the CB bottom and below the VB top, respectively. It can be seen from table 1 that the mobility bandgap values of all the three aTiO₂ models are in good agreement with the experimental data. The bandgap values obtained from DFT + U in the present study are closer to the experimental data as compared to the DFT results reported here as well as in reference (Prasai *et al* 2012). It is noted that, due to a large number of levels with different IPRs in the top of the VB and bottom of the CB, there is some uncertainty in defining the gap. For a given energy state in the VB and CB, the localization is observed to occur on more than one atom as also observed in amorphous GaN (Cai and Drabold 2011, Stumm and Drabold 1996).

To correlate the electronic structure with topological units, electronic states with relatively high IPR were picked for the 96-atom model and projected onto individual atom sites. For the sake of simplicity only the Γ point is considered for this analysis. There are five Ti atoms and six O atoms that are mainly associated with the localized CB and VB tail states, respectively. Out of these five Ti atoms, two are six-fold coordinated, another two are four-fold coordinated, and the last one is two-fold coordinated. Out of the six O atoms, two are three-fold coordinated, three are two-fold coordinated, and the last one is one-fold coordinated. It is also notable that

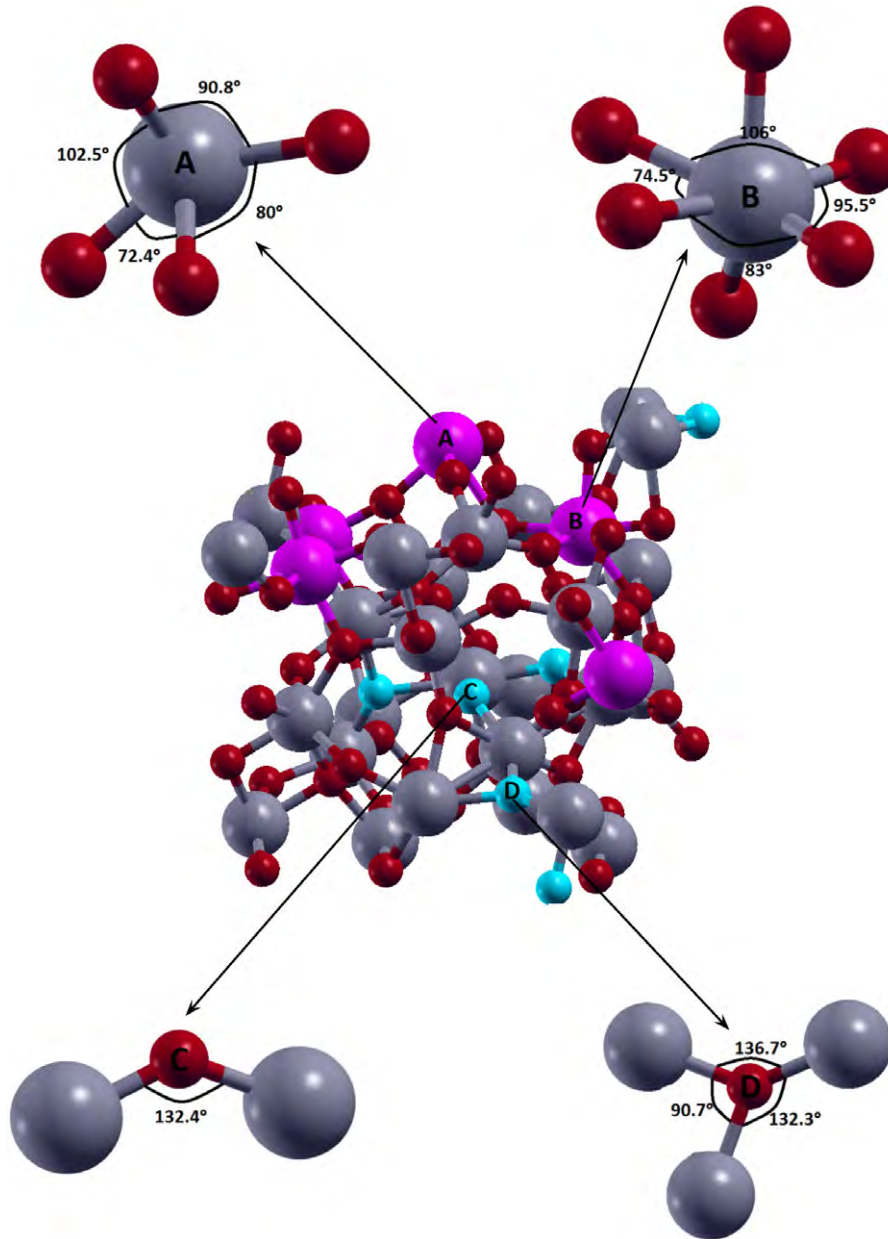


Figure 4. Atomistic origin of electronic tail states correlated with higher IPR states indicated in figure 3(b) for the 96-atom model. Atoms which have major contributions to highly localized states at the VB and CB tail of the 96-atom model (figure 3(b)) are marked in cyan and pink colors respectively. Gray atoms represent Ti; red atoms represent O.

the major contribution to highly localized states at the CB and VB tails comes from only two Ti (atom A and atom B) and two O (atoms C and atom D) atoms, respectively. Atoms A, B, C and D are represented in figure 4. The four nearest neighbors of atom A form distorted $\angle\text{Ti-O-Ti}$ of 80° , 90.8° , 102.5° and 72.4° , respectively. Out of six neighbors of atom B, four are almost coplanar forming $\angle\text{Ti-O-Ti}$ of 106° , 95.5° , 83° and 74.5° , respectively. The two nearest neighbors of atom C form $\angle\text{Ti-O-Ti}$ of 132.4° , and the three nearest neighbors of atom D form $\angle\text{Ti-O-Ti}$ of 136.7° , 132.3° and 90.7° . Prasai *et al* (2012) have reported previously that the highly localized tail states at VB and CB are due to the displaced O atoms and over-coordinated Ti atoms, respectively. In contrast, our study suggests that the positional disorder of O and Ti atoms

and a significant amount of planar distortion due to under- and over-coordinated Ti and O atoms actually leads to the localization of tail states. This difference in the origin of localized states between the present study and the previously mentioned analysis (Prasai *et al* 2012) may be due to a difference in the intrinsic short range order of disordered systems and a difference in the sample preparation method used.

3.2. Monodoped aTiO₂

The electronic DOS and electronic localization of aTiO₂ are quite insensitive to the variation in local disorder among models. The analysis of the electronic properties suggests

that the electronic properties of aTiO₂ are similar to that of cTiO₂ despite the local disorder present in aTiO₂. This encouraging observation suggests the possibility of using aTiO₂ as an alternative to cTiO₂. However, it is recognized that due to the disorder present in aTiO₂, it may have a lower efficiency. Doping has proven beneficial in enhancing the visible light photocatalytic activity of cTiO₂ due to a bandgap reduction. Furthermore, it is reported that for doped amorphous semiconductors, the relative position of impurity atoms determines the mid-gap energy states, and the effect of the structure of the host amorphous system is relatively minor (Kadas and Kugler 2002). Therefore, it is expected that the photocatalytic behavior of aTiO₂ can be improved via appropriate doping.

To investigate this, monodoping with n-type and p-type dopants was conducted. From the IPR plot for undoped aTiO₂, shown in figure 3(b), it can be observed that there is asymmetry in the width and the localization of the tail states for aTiO₂. As reported for the case of GaN (Cai and Drabold 2011), if the VB tail states are more localized as compared to the CB tail states, it would be more difficult to move the Fermi level towards the valence edge, leading to poor mobility. Therefore, to obtain an identical carrier concentration, p-type doping of aTiO₂ is expected to be more difficult than n-type doping. N is chosen here as the p-type dopant because it has higher atomic p orbital energy than O to form acceptor impurity levels above the VB minima, which reduces the photo-transition energy. On the other hand, Nb is chosen as the n-type dopant because it exhibits high 4d atomic orbital energy, and therefore is more likely to transfer its excess electron to the CB maxima of the host aTiO₂ without lowering the CB minimum energy level (Ma *et al* 2011).

3.2.1. N-doped aTiO₂. In previous studies of N-doped rutile TiO₂ (Yang *et al* 2006, Varley *et al* 2011), the lowest-energy structure for substitutional N was shown to have the dopant at the position of a missing O atom. Assuming that it holds true for aTiO₂ as well, and also to enable direct comparison with cTiO₂, one N atom was substituted in the position of O in the 96-atom model of aTiO₂. The total DOS and PDOS for the p electrons of N and O atoms and d electrons of Ti atoms of N-doped aTiO₂ are summarized in figure 5(a). The PDOS plot shows that the p states of N atom influence the energy band structure of aTiO₂. It can also be inferred from this figure that the defect states are present mainly due to the contribution from N atoms. To understand this further, consider the electronic configuration of the N atom which is 2s²2p³ and the O atom which is 2s²2p⁴. The substitution of N in the place of O in aTiO₂ results in an unstable oxidation state of -2 (2s²2p⁵). Thus, to obtain the stable oxidation state of -3, N-doping increases the asymmetry between the neighboring atoms by introducing an unpaired p electron. This is depicted in the spin density plot (figure 5(b)). N-doping decreases the energy bandgap of the system by introducing an energy state at the tail of VB maxima. The upshift of VB maxima is 0.25 eV which leads to Γ point energy gap of about 2.25 eV. It is interesting to note that this behavior of N-doped aTiO₂ is similar to N-doped anatase but not to N-doped rutile

TiO₂. In N-doped rutile, the band tail at the VB maxima does not exist (Ma *et al* 2011, Tsetseris 2011). N-doping in aTiO₂ also results in 0.3 eV wide intermediate energy band, found 0.95 eV below the bottom of the CB. These mid-bandgap states have also been observed in N-doped crystalline TiO₂ phases (Yang *et al* 2006, Tsetseris 2011, Zhao and Liu 2008). The IPR plot for N-doped aTiO₂, depicted in figure 5(c) suggests that the localization of energy states increases for N-doped aTiO₂ as compared to undoped aTiO₂. Due to N-doping the charge is highly localized at the mid-gap energy states, 1.0 eV below the bottom of the CB and just above the VB maxima of host aTiO₂. This localization is due to N 2p states, as the bandgap states and top of the VB maxima mainly consist of N 2p states, as shown in figure 5(a). The charge localization at CB tail states is more pronounced in N-doped aTiO₂ as compared to undoped aTiO₂, which leads to a reduction in charge migration. Furthermore, the position of the Fermi level indicates that N-doped aTiO₂ can trap only one type of carrier (holes) which is ineffective because the immobile charge species would then quickly recombine with its mobile counterpart leading to more recombination centers than trapping centers (Choi *et al* 1994).

3.2.2. Nb-doped aTiO₂. To analyze the effect of n-type doping of aTiO₂, one Nb atom is substituted in the position of a Ti atom. The total DOS and PDOS for the d electrons of Nb and Ti atoms and p electrons of O atoms are shown in figure 6(a). The substitution of Ti atom with Nb in aTiO₂ results in a narrow peak of width 0.3 eV in the bandgap, 0.5 eV below the CB edge. The PDOS plot suggests that this defect state is mainly due to contributions from Ti atoms. These results are quite similar to Nb-doped cTiO₂. For crystalline TiO₂ phases, Nb doping shows a defect state in the bandgap that is well separated from the CB (Morgan *et al* 2009, Morris *et al* 2000). Considering the electronic configuration of Nb: 4p⁶4d³5s², substitution of Ti by Nb should result in the Nb⁴⁺ state, i.e. 4p⁶4d¹5s⁰ configuration. Thus, to obtain a stable oxidation state of +5 the extra electron from Nb⁴⁺ is preferentially transferred to Ti⁴⁺, and therefore the Ti³⁺ state is formed. The electron transfer from the Nb to Ti species is also apparent from the spin density plot shown in figure 6(b) where a strong localization of spin density on the Ti atoms in the nearest neighbor position can be observed. The IPR analysis depicted in figure 6(c) suggests that the charge is highly localized 0.5 eV below the bottom of the CB of the host aTiO₂ and just above the VB maxima. This would lead to a reduction in the charge migration. Furthermore, the position of the Fermi level suggests that in Nb-doped aTiO₂, only one type of carrier (electrons) can be trapped, which will lead to the formation of recombination centers as explained in section 3.2.1.

Overall, monodoping of aTiO₂ with N or Nb leads to dopant states at the VB maxima and an intermediate band with considerable bandwidth. The intermediate band offers a stepping stone for the absorption of low energy photons. The electrons at the VB maximum get excited to the intermediate bands, from where they can be excited again above the CB, thus improving the photoactivity of aTiO₂. This opens up

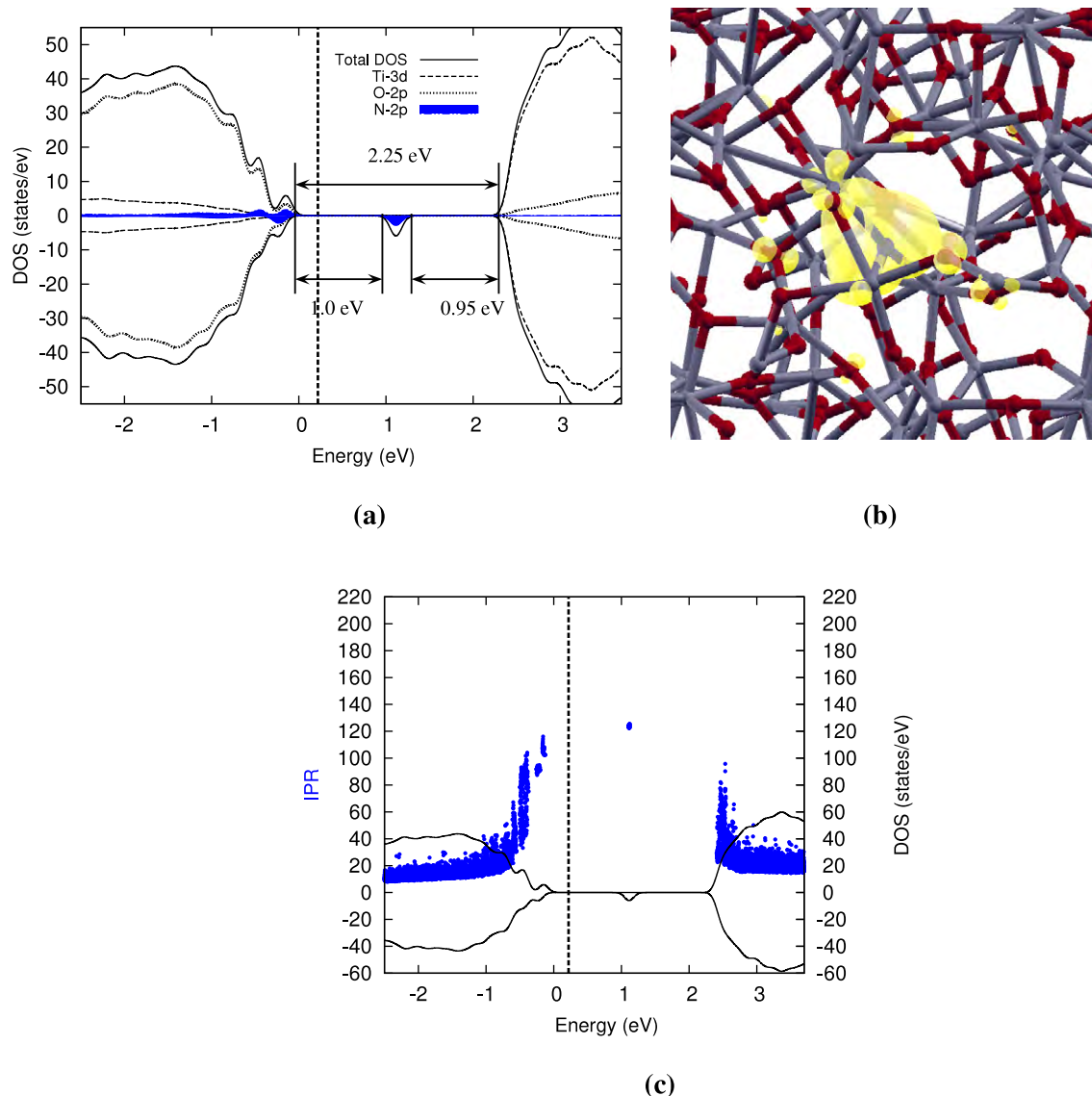


Figure 5. (a) The total DOS and PDOS for p and d orbitals, (b) spin density and (c) the total density of states (black line, right scale) and the corresponding values of the IPR (blue dots, left scale) for the N-doped aTiO₂ model. The zero energy value is set at the top of VB and Fermi energy is represented by the vertical dashed line in (a) and (c).

the possibility of doped aTiO₂ for visible light photocatalytic applications. However, IPR analysis shows that the band tail states are more localized in doped aTiO₂ than undoped aTiO₂. These localized mid-gap states can promote recombination of electron-hole pairs (Irie *et al* 2003, Choi *et al* 1994) and can reduce charge carrier mobility. Consequently, monodoping of aTiO₂ by N or Nb is not expected to improve its photocatalytic performance appreciably.

3.3. Codoped aTiO₂

The bandgap states which can act as recombination centers (Niishiro *et al* 2007) render monodoped aTiO₂ an ineffective photocatalyst. For crystalline TiO₂ phases, it has already been established that the elimination of the bandgap states can be achieved by charge compensated codoping (Niishiro *et al* 2007, Long and English 2011). Taking motivation from these

studies, codoping of aTiO₂ with N and Nb was investigated with the hope of eliminating recombination centers, through the mechanism of charge compensation. To study the codoped aTiO₂ system, three nearest neighbor structures having N-Nb distances of 2.07, 2.02 and 1.84 Å were constructed (figure 7). These structures were relaxed to obtain the most stable configuration for the codoped system. The structure having N-Nb distance of 2.07 Å showed the lowest configurational energy and is therefore considered for further analysis. In order to understand whether the codoped structure is more stable than the monodoped structures, analysis was carried out with a supercell where N and Nb dopants were well separated in space (3.42 Å). This showed that the codoped structure has a lower energy when N and Nb occupy neighboring positions, with the most stable codoped configuration having an energy 0.83 eV lower than the configuration with larger N-Nb distance.

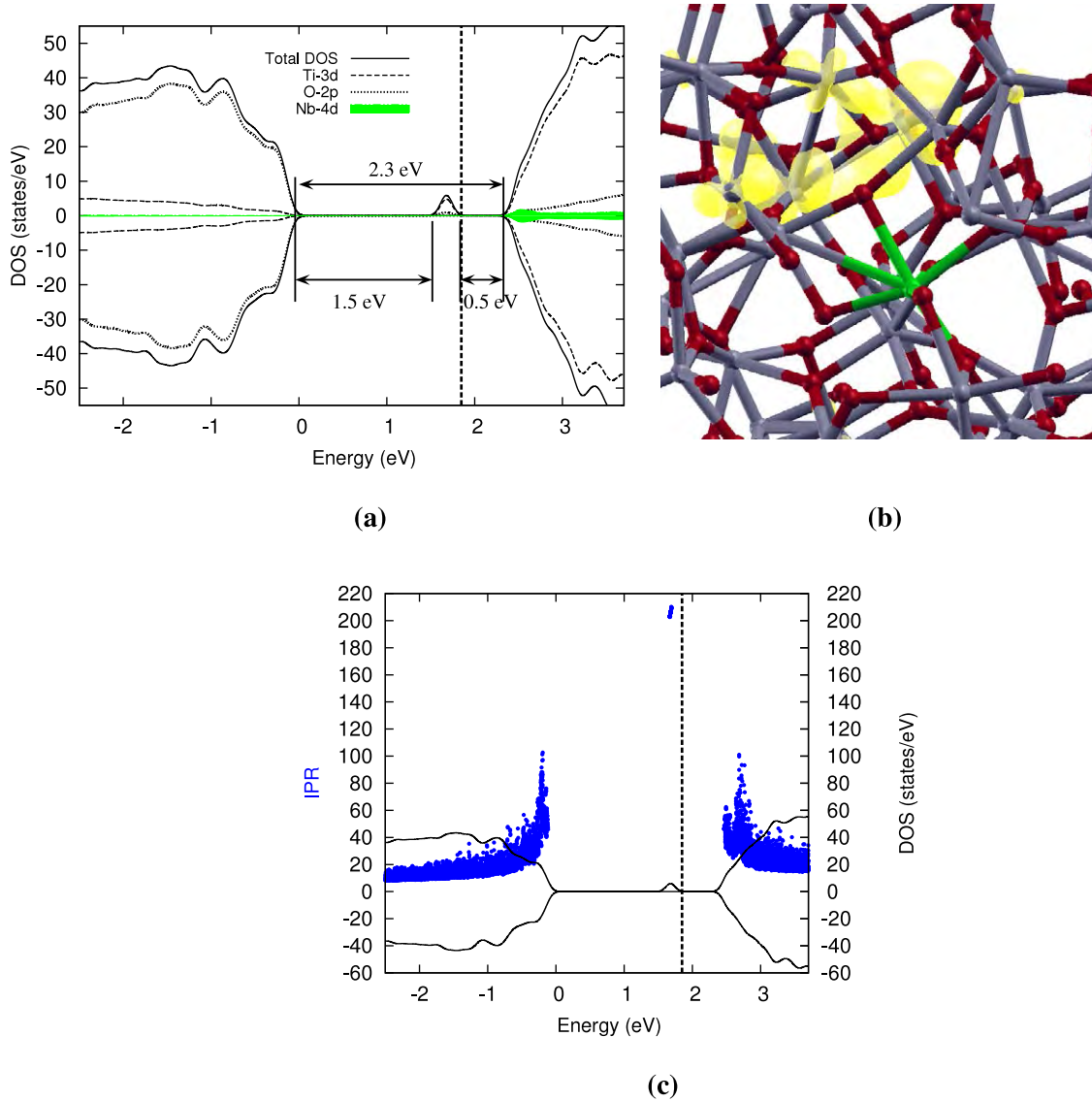


Figure 6. (a) The total DOS and PDOS on the p and d orbitals, (b) spin density, and (c) the total DOS (black line, right scale) and the corresponding values of the IPR (blue dots, left scale) for Nb-doped aTiO₂ model. The zero energy value is set at the top of VB and Fermi energy is represented by the vertical dashed line in (a) and (c).

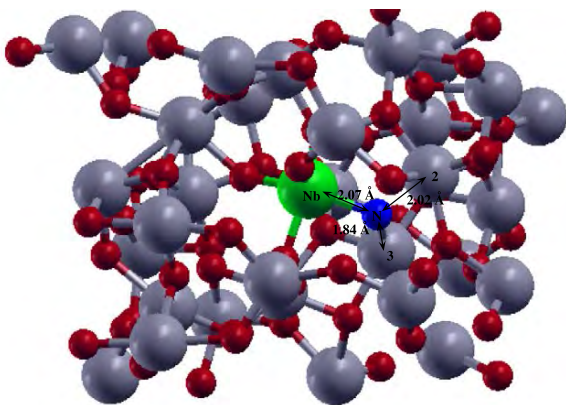


Figure 7. The 96-atom model of (N, Nb)-codoped aTiO₂. Ti, O, N and Nb atoms are highlighted in gray, red, blue and green respectively. The three nearest neighboring positions considered for Nb atom are shown along with dopant–dopant distances.

Total spin polarized DOS and PDOS for the d electrons of Nb and Ti atoms and p electrons of N and O atoms of the (N, Nb)-codoped aTiO₂ are depicted in figure 8(a). The codoping reduces the bandgap by 0.4 eV relative to undoped TiO₂. This is due to the hybridized N and O 2p states at the top of the VB maxima which results in decreased bandgap energy without affecting the CB level. In order to understand the nature of codoping consider the electronic configurations of N and Nb. As described previously in the analysis of N and Nb monodoping, N dopant requires an extra electron to achieve the stable -3 oxidation state whereas Nb dopant introduces an extra electron into the system. Thus, when aTiO₂ is codoped with N and Nb, the extra electron required by N atom is transferred from Nb such that the N species attains a -3 state ($2s^2 2p^6$), while the Nb species attains a $+5$ ($4p^6 4d^0 5s^0$) state. Codoping of aTiO₂ with N and Nb thus leads to stable configurations for both N and Nb atoms. For further quantitative understanding of this behavior, the Bader

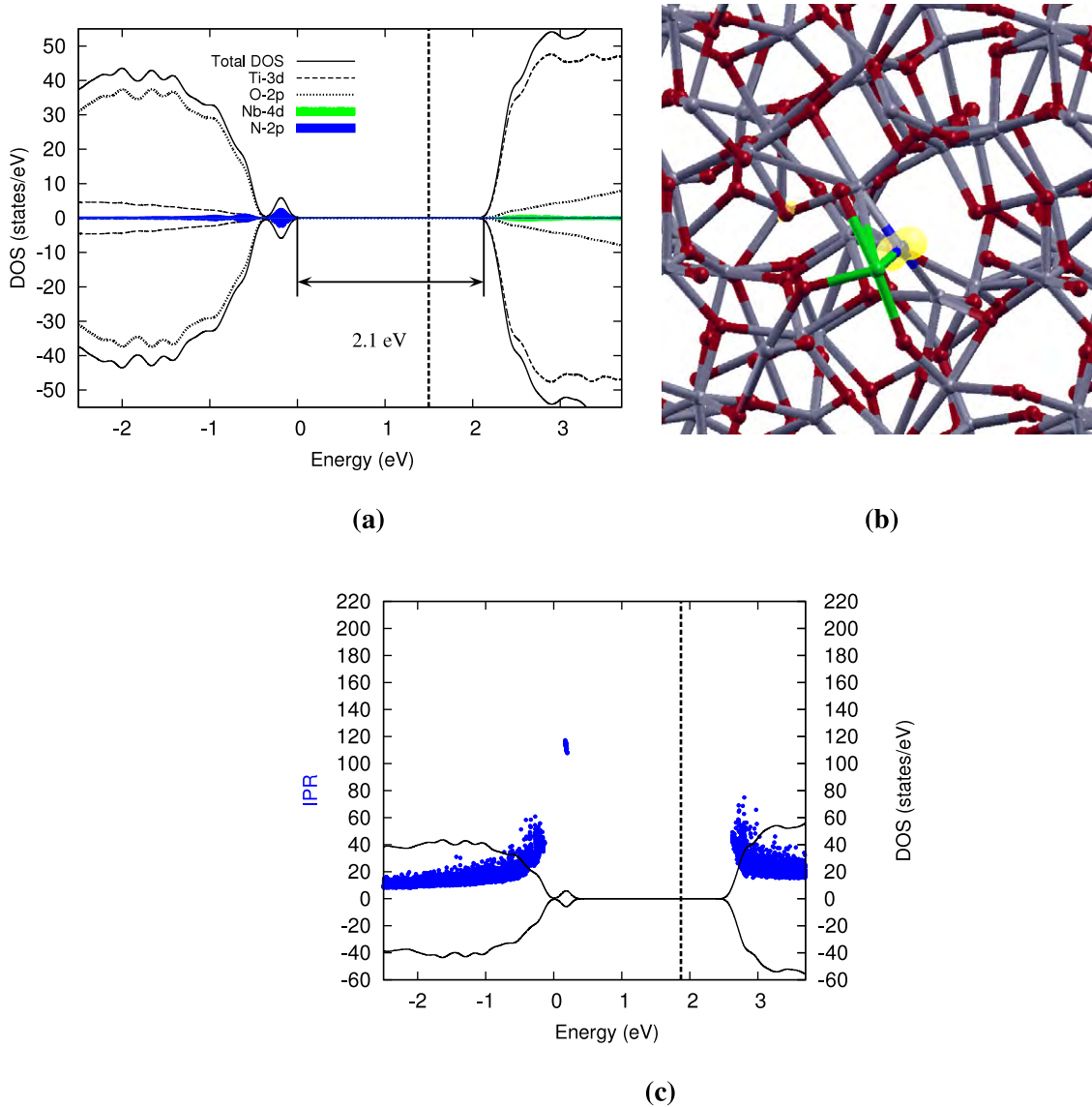


Figure 8. (a) The total DOS and PDOS for p and d orbitals, (b) spin density, and (c) the total DOS (black line, right scale) and the corresponding values of the IPR (blue dots, left scale) for (N, Nb)-codoped aTiO₂. The zero energy value is set at the top of the VB and the Fermi energy is represented by the vertical dashed line in (a) and (c).

charge analysis based on the atom in molecule (AIM) theory (Celik and Mete 2012) was performed using a grid based decomposition algorithm (Tang *et al* 2009). The oxidation state of Nb is +2.6602e in Nb-doped aTiO₂ which is similar to the oxidation states of Nb (= +2.6088e) in (N, Nb)-codoped aTiO₂. The charge on Nb remains the same as it transfers the same charge (formal charge = 1 electron) to Ti in both N-doped and (N, Nb)-codoped aTiO₂ and attains the formal charge of +5. However, the oxidation state of N is -1.0642 in N-doped aTiO₂ and -1.3645 (i.e. more negative) in (N, Nb)-codoped aTiO₂. This explains why N has an unstable oxidation state (a formal charge of -2) in N-doped TiO₂, while it achieves a more stable oxidation state (-3) in the case of the (N, Nb)-codoped system.

The comparison of the DOS curves of monodoped and codoped aTiO₂ systems suggests that the bandgap states for the monodoped systems (figures 5(a) and 6(a)) are too deep in

the forbidden gap and do not overlap sufficiently with the band states of aTiO₂. This leads to localization of photogenerated carriers. On the other hand, in the charge-compensated codoped system, the acceptor states shift towards the VB edge while the donor states shift towards the CB edge (figure 8(a)). This enhances coupling between the donor states and O 2p states, and between the acceptor states and the CB, resulting in the formation of delocalized holes and electrons, respectively (Chen *et al* 2010). However, the contribution of Nb 4d states is less pronounced than the N 2p states in aTiO₂, leading to shallow energy states just above the VB maxima. This leads to a less balanced configuration, both geometrically and electronically. This behavior of codoped aTiO₂ is slightly different than the corresponding codoped system for crystalline TiO₂. In (N, Nb)-codoped anatase, Nb 4d states lower the energy levels of N 2p states, bringing the N 2p states much closer to the VB and therefore, enhancing the

mixing of N2p and O2p states in the VB leading to continuum states (Ma *et al* 2011). These shallow acceptor and donor states can significantly accelerate the mobility of the trapped charges, causing rapid transportation of the photogenerated carriers in the codoped aTiO₂ as compared to the systems considered here.

The charge compensation of the (N, Nb)-codoped system can also be inferred from the absence of excess spin density states in the plot depicted in figure 8(b). The same observation can be drawn from a decrease in localization of VB and CB tail states in codoped aTiO₂ as displayed in figure 8(c). A decrease in the localization of host aTiO₂ states promotes the separation of electron and hole pairs excited under visible-light irradiation. Overall, this analysis suggests that there is a smaller degree of defectiveness in the codoped structure as compared to monodoped structures. Localization at band tails in codoped aTiO₂ is not only less pronounced than both monodoped systems but also lower than undoped aTiO₂ and this makes codoped aTiO₂ more efficient than both undoped and monodoped systems. However, a complete elimination of the localized states has not been achieved. Codoping, nonetheless, suggests a way forward in improving the efficiency of aTiO₂ and should be investigated further, both theoretically and experimentally, along with other dopants.

4. Conclusions

Due to the recent interest in disordered and amorphous TiO₂, there has been a need to theoretically analyze its electronic properties and explore doping as a means of optimizing the photocatalytic properties. In this paper, *ab initio* calculations using the DFT + *U* approach were conducted to analyze and understand the effects of doping on the electronic structure and the photocatalytic behavior of aTiO₂. The analysis of the structural and electronic properties of undoped aTiO₂ suggests that the localization of band tail states in aTiO₂ is due to a significant amount of planar distortion as well as under- and over-coordinated Ti and O atoms. Monodoping aTiO₂ with either N or Nb leads to a slight reduction in the bandgap as well as deep states in the bandgap. These mid-gap states can act as stepping stones for electrons to jump from VB to CB but also can lead to an increase in recombination centers. Also, N or Nb doping increases localization of host aTiO₂ leading to reduced charge migration. The charge compensated (N, Nb)-codoping of aTiO₂ decreases the energy gap by 0.4 eV and suppresses the recombination of electron–hole pairs by eliminating the bandgap states and reducing the localization of energy states of host aTiO₂. Thus, our analysis establishes the beneficial aspects of charge compensated codoping in aTiO₂, similar to what has been established in previous reports of crystalline TiO₂.

The significant finding of this study is that the low photocatalytic efficiency of aTiO₂ due to a large bandgap and reduced charge migration can be circumvented by appropriate charge compensated codoping. If this can also be achieved experimentally, aTiO₂ may prove as an alternative to cTiO₂. However, in order to fully attain more effective delocalization

of the energy states present in aTiO₂, further investigation with various types of dopants is necessary. Furthermore, size effects may be appreciable, especially for the band tail properties. Hence, a more detailed investigation with a much larger simulation cell may be desired in future to reduce any intrinsic size effect present in this study.

Acknowledgments

The authors would like to thank the Natural Sciences and Engineering Research Council of Canada (NSERC) and the University of Toronto for providing funding for this research. Computations were performed at SciNet (Loken *et al* 2010) and Calcul Quebec consortia under the auspices of Compute Canada. SciNet is funded by the Canada Foundation for Innovation, the Government of Ontario, Ontario Research Fund—Research Excellence, and the University of Toronto. The authors gratefully acknowledge the continued support of the above organizations.

References

- Amtout A and Leonelli R 1995 *Phys. Rev. B* **51** 6842
 Buddee S, Wongnawa S, Sirimahachai U and Puetpaibool W 2011 *Mater. Chem. Phys.* **126** 167
 Cai B and Drabold D A 2011 *Phys. Rev. B* **84** 075216
 Celik V and Mete E 2012 *Phys. Rev. B* **86** 205112
 Chen X, Liu L, Yu P Y and Mao S S 2011 *Science* **331** 746
 Chen C, Ma W and Zhao J 2010 *Curr. Org. Chem.* **14** 630
 Choi W Y, Termin A and Hoffmann M R 1994 *J. Phys. Chem.* **98** 13669
 Fedders P A, Drabold D A and Nakhmanson S 1998 *Phys. Rev. B* **58** 15624
 Fennell C and Gezelter J 2006 *J. Chem. Phys.* **124–136** 234104
 Ghuman K K and Singh C V 2013 *J. Phys.: Condens. Matter* **25** 085501
 Giannozzi P *et al* 2009 *J. Phys.: Condens. Matter* **21** 395502
 Han C H H, Lee H S, Lee K W, Han S D and Singh I 2009 *Bull. Korean Chem. Soc.* **30** 219
 Irie H, Watanabe Y and Hashimoto K 2003 *J. Phys. Chem. B* **107** 5483
 Justo J F, Mota F D B and Fazio A 2002 *Phys. Rev. B* **65** 073202
 Kadas K and Kugler S 2002 *J. Optoelectron. Adv. Mater.* **4** 455
 Kanna M and Wongnawa S 2008 *Mater. Chem. Phys.* **110** 166
 Kaur K, Prakash S and Goyal N 2011 *J. Mater. Res.* **26** 2604
 Kaur K and Singh C V 2012 *Energy Procedia* **29** 291
 Li J, Liu S, He Y and Wang J 2008 *Micropor. Mesopor. Mater.* **115** 416
 Loken C *et al* 2010 *J. Phys.: Conf. Ser.* **256** 012026
 Long R and English N J 2011 *Phys. Rev. B* **83** 155209
 Ma X, Wu Y, Lu Y, Xu J, Wang Y and Zhu Y 2011 *J. Phys. Chem. C* **115** 16963
 Manzini I, Antanioli G, Bersani D, Lottici P P, Gnappi G and Montonero A 1995 *J. Non-Cryst. Solids* **192** 519–23
 Matsui M and Akaogi M 1991 *Mol. Simul.* **6** 239
 Möller J S, Henrik H K, Hinnemann B, Madsen G K H and Hammer B 2010 *J. Chem. Phys.* **133** 144708
 Monkhorst H J and Pack J D 1976 *Phys. Rev. B* **13** 5188
 Morgan B J, Scanlon D O and Watson G W 2009 *J. Mater. Chem.* **19** 5175
 Morgan B J and Watson G W 2007 *Surf. Sci.* **601** 5034
 Morris D, Dou Y, Rebane J, Mitchell C E, Egdell R G, Law D S L, Vittadini A and Casarin M 2000 *Phys. Rev. B* **61** 13445
 Mott N F and Davis E A 1979 *Electronic Processes in Non-Crystalline Materials* 2nd edn (Oxford: Clarendon)

- Niishiro R, Konta R, Kato H, Chun W J, Asakura K and Kudo A 2007 *J. Phys. Chem. C* **111** 17420
- Ohtani B, Ogawa Y and Nishimoto S I 1997 *J. Phys. Chem. B* **101** 3746
- Perdew J, Burke K and Ernzerhof M 1996 *Phys. Rev. Lett.* **77** 3865
- Petkov V, Holzhuter G, Tronge U, Gerber T and Himmel B 1998 *J. Non-Cryst. Solids* **231** 17
- Prasai B, Cai B, Underwood M K, Lewis J P and Drabold D A 2012 *J. Mater. Sci.* **47** 7515
- Rahman M, MacElroy D and Dowling D P 2011 *J. Nanosci. Nanotechnol.* **11** 8642
- Rino J P and Studart N 1999 *Phys. Rev. B* **59** 6643
- Sanchez-Portal D, Artacho E and Soler J M 1995 *Solid State Commun.* **95** 685
- Smith W and Todorov I T 2006 *Mol. Simul.* **32** 935
- Stumm P and Drabold D A 1996 *J. Appl. Phys.* **81** 1289
- Tang H, Berger H, Schmid P E, Levy F and Burri G 1993 *Solid State Commun.* **87** 847
- Tang W, Sanville E and Henkelman G 2009 *J. Phys.: Condens. Matter* **21** 084204
- Thomas A G *et al* 2007 *Phys. Rev. B* **75** 035105
- Tsetseris L 2011 *Phys. Rev. B* **84** 165201
- Valencia S, Marín J and Restrepo G 2010 *Open Mater. Sci.* **4** 9
- Vanderbilt D 1990 *Phys. Rev. B* **41** 7892
- Varley J B, Janotti A and van de Walle C G 2011 *Adv. Mater.* **23** 2343
- Wendt S *et al* 2008 *Science* **320** 1755
- Yang K, Dai Y, Huang B and Han S 2006 *J. Phys. Chem. B* **110** 24011
- Zhang Z and Maggard P A 2007 *J. Photochem. Photobiol. A* **186** 8
- Zhao Z and Liu Q 2008 *J. Phys. D: Appl. Phys.* **41** 025105